C-band Scatterometer (CScat): the first global long-term satellite radar backscatter data set with a C-band signal dynamic

Shengli Tao[1*], Zurui Ao[2*], Jean-Pierre Wigneron[3], Sassan Saatchi[4], Philippe Ciais[5], Jérôme Chave[6], Thuy Le Toan[7], Pierre-Louis Frison[8], Xiaomei Hu[1], Chi Chen[9], Lei Fan[10], Mengjia Wang[11], Jiangling Zhu[1], Xia Zhao[12], Xiaojun Li[3], Xiangzhuo Liu[3], Yanjun Su[12], Tianyu Hu[12], Qinghua Guo[13], Zhiheng Wang[1], Zhiyao Tang[1], Yi Y. Liu[14*], Jingyun Fang[1]

[1] Institute of Ecology, College of Urban and Environmental Sciences, and Key Laboratory for Earth Surface Processes of the Ministry of Education, Peking University, Beijing 100871, China
[2] Beidou Research Institute, Faculty of Engineering, South China Normal University, Foshan 528000, China
[3] ISPA, UMR 1391, Inrae Nouvelle-Aquitaine, Université de Bordeaux, Grande Ferrade, Villenave d'Ornon, France
[4] Jet Propulsion Laboratory, California Institute of Technology, Pasadena, CA, 91109, USA
[5] Laboratoire des Sciences du Climat et de l'Environnement/IPSL, CEA-CNRS-UVSQ, Université Paris Saclay, Gif-sur-Yvette, France
[6] CNRS, Université Toulouse 3 Paul Sabatier, IRD, UMR 5174 Evolution et Diversité Biologique (EDB), 31062 Toulouse, France
[7] Centre d'Etudes Spatiales de la Biosphère, CNRS-CNES-UPS-IRD, Toulouse, France
[8] LaSTIG, Université Gustave Eiffel, ENSG, IGN, F-77420 Champs-sur-Marne, France
[9] Climate and Ecosystem Sciences Division, Lawrence Berkeley National Laboratory, Berkeley, CA 94720
[10] Chongqing Jinfo Mountain Karst Ecosystem National Observation and Research Station, School of Geographical Sciences, Southwest University, Chongqing 400715, China
[11] School of Geoscience and Technology, Zhengzhou University, 450001, China
[12] State Key Laboratory of Vegetation and Environmental Change, Institute of Botany, Chinese Academy of Sciences, Beijing, 100093, China
[13] Institute of Remote Sensing and Geographical Information Systems, School of Earth and Space Sciences, Peking University, Beijing 100871, China
[14] School of Civil and Environmental Engineering, University of New South Wales, Sydney NSW 2052, Australia

Correspondence to: Shengli Tao (sltao@pku.edu.cn), Zurui Ao (aozurui@m.scnu.edu.cn), Yi Y. Liu (yiliu001@gmail.com)

Abstract Satellite radar backscatter contains unique information on land surface moisture, vegetation features, and surface roughness, and can be acquired in all weather conditions, thus has been used in a range of earth science disciplines. However, there is no single global radar data set that spans more than two decades. This has limited the use of radar data for trend analysis over extended time intervals. We here provide the first long-term (since 1992), high resolution (~8.9 km) satellite radar backscatter data set over global land areas, the C-band Scatterometer (CScat) data set, by fusing signals from European Remote Sensing satellite (ERS, 1992-2001, C-band, 5.3 GHz), Quick Scatterometer (QSCAT, 1999-2009, Ku-band, 13.4 GHz), and the Advanced Scatterometer (ASCAT, since 2007, C-band, 5.255 GHz).

The six-year data gap between C-band ERS and ASCAT was filled out by modelling an equivalent C-band signal during 1999-2009 from Ku-band QSCAT signals and climatic information. Towards this purpose, we first rescaled the signals from different sensors, pixel by pixel, using a new signal rescaling method that is robust to limited overlapping observations among sensors. We then corrected the monthly signal differences between the C-band and the scaled Ku-band signals, by modelling the signal differences from climatic variables (i.e., monthly precipitation, skin temperature, and snow depth) using decision tree regression.

The quality of the merged radar signal was assessed by computing the Pearson r, Root Mean Square Error (RMSE), and relative RMSE (rRMSE) between the C-band and the corrected Ku-band signals in the overlapping years (1999-2001 and 2007-2009). We obtained high Pearson r values and low RMSE values at both the regional ($r \geqslant 0.93$, RMSE $\leqslant 0.16$, rRMSE $\leqslant 0.37$) and pixel levels (median r across pixels $\geqslant 0.80$, median RMSE $\leqslant 0.38$, median rRMSE $\leqslant 0.64$), suggesting high accuracy for the data merging procedure.

The merged radar signal was then validated with a continuous ERS-2 data set available between 1995 and 2011. ERS-2 stopped working in full mode after 2001 but observations are occasionally available for a subset of the pixels until 2011. Because the period of 1995-2011 fully overlaps with the working period of QSCAT (1999-2009), comparing the merged radar signal against the ERS-2 data in 1995-2011 is the most direct validation available. We found concordant monthly dynamics between the merged radar signals and the ERS-2 signals during 1995-2011, with Pearson r value ranging from 0.79 to 0.98 across regions. These results evidenced that our merged radar data have a consistent C-band signal dynamic.

The CScat data set (https://doi.org/10.6084/m9.figshare.20407857, Tao et al. 2022a) is expected to advance our understanding of the long-term changes in, e.g., global vegetation and soil moisture. The data set will be updated on a regular basis.

1 Introduction

Microwave remote sensing uses electromagnetic radiation with a wavelength (λ) between 1 cm and 1 m as a measurement tool (Ulaby et al. 1982). Depending on the source of the energy from which information is gathered, microwave remote sensing systems can be categorized into two groups: passive (radiometer) and active (radar). Passive systems collect the radiation naturally emitted by the observed surface, whereas active systems transmit a (radio) signal in the microwave bandwidth and record the signal backscattered by the target (Ulaby et al., 2014).

Due to the longer wavelength compared to visible and infrared radiation, microwaves exhibit the important property of penetrating objects, with the penetrating ability increasing with increasing wavelength. Microwaves at high frequencies (such as Ku-band, ~13 GHz, $\lambda = $~2 cm) are sensitive to atmospheric conditions, but those at lower frequencies, such as C-band radio frequency (~5 GHz, $\lambda = $~6 cm), depend less on cloud cover and heavy rain events, making this technique suitable to work in all weather conditions (Ulaby et al., 2014; Carabajal and Harding, 2006; Le Toan et al., 2011). As a result, long-wavelength microwave remote sensing has been widely used in earth science studies for atmosphere, land, and ocean monitoring (Wentz et al., 1992; Wagner et al., 1999; Spreen et al., 2008; Wagner et al., 2007; Shi et al., 2016; Steele-Dunne et al., 2017; Murfitt and Duguay, 2021).

However, there is no single multi-decadal microwave data set acquired at C-band or longer wavelength that spans more than two decades. This has limited the use of microwave data for trend analysis over extended time intervals. Several passive microwave systems are available, such as the Advanced Microwave Scanning Radiometer for EOS (AMSR-E, 2002-2011), The Advanced Microwave Scanning Radiometer 2 (AMSR2, 2012-now), WindSat (2003-2012), Soil Moisture and Ocean Salinity (SMOS, 2010-now) and Soil Moisture Active Passive (SMAP, 2015-now), all of which providing data with a wavelength of ~6 cm or longer (Spreen et al., 2008; Yao et al., 2021; Wigneron et al., 2017; Wigneron et al., 2020; Wigneron et al., 2021). However, merging them into a harmonized data set with a timespan longer than two decades has been shown to be challenging, mainly because AMSR-E has no overlapping observations with AMSR2 (Du et al., 2017; Moesinger et al., 2020; Wang et al., 2021).

Active microwave remote sensing, or radar, has the potential to overcome this limitation. Scatterometer is one type of radars known for its large footprint, global coverage and high revisit rate. These properties make scatterometers interesting for the study of large-scale land surface dynamics (Ulaby et al., 2014). Spaceborne scatterometer sensors have been deployed since 1978 (NASA's Seasat, Ku-band), but global coverage of scatterometer observation dates back to the European Remote Sensing satellite (ERS) in the 1990s (C-band, from 1992 to 2001; Frison and Mougin, 1996; Lecomte and Wagner, 1998; Prigent et al., 2001). Over the past three decades, multiple scatterometer missions have been launched with the aim of obtaining full and repeated global coverage (Ulaby et al., 2014), such as the Quick Scatterometer (QSCAT, Ku-band, from 1999 to 2009), the

Oceansat-2 Scatterometer (OSCAT, Ku-band, since 2009), and the Advanced Scatterometer (ASCAT, C-band, from 2007 to 2018). Among these sensors, both ERS and ASCAT operate at the C-band frequency, but have a temporal gap of about six
100 years (i.e., between 2001 and 2007). Filling this time gap would lead to the first global C-band scatterometer data set with continuous observations for the past three decades (since 1992). Moreover, this data set could in principle be further extended because ASCAT is still operational, and similar C-band radar missions are secured in the future (such as the Sentinel radar series; Malenovský et al., 2012).

105 The present study aims at filling up the six-year gap of the C-band scatterometer data using Ku-band QSCAT data at the global scale (Fig. 1). QSCAT operated between 1999 and 2009, thus overlapping with both ERS (between 1999 and 2001) and ASCAT (between 2007 and 2009). In theory, the Ku-band signal interacts more with smaller elements (such as raindrops, snows, and canopy leaves) than the C-band signal, due to the difference in wavelength (Saatchi et al., 2013). However, we have previously found that the Ku-band QSCAT signal can be adjusted to the ERS observations during 1999–2001 and to the
110 ASCAT observations during 2007–2009 to obtain a simulated C-band signal (Tao et al., 2022b). Our previous approach was especially designed for global tropical areas. Here, we further improved the method through a better understanding of the signal differences across climatic gradients, and by developing a new signal rescaling method. We then applied the improved method at the global scale. Image resolution has also been enhanced: while the native resolution of scatterometer images is often coarse (25 km or larger), the National Aeronautics and Space Administration (NASA) Scatterometer Climate Record
115 Pathfinder (SCP, www.scp.byu.edu/) project has improved the resolutions of ERS, QSCAT, and ASCAT images using the Scatterometer Image Reconstruction (SIR) with Filtering (SIRF) algorithm (Long et al. 1993; Early & Long 2001). Specifically, ERS images of 8.9 km resolution in the period of 1992-2001, and QSCAT (1999-2009) and ASCAT (2007-now) images of 4.45 km resolution have been made publicly available. For guaranteeing a long time-span since 1992, we chose to perform the data merging method at the resolution of ERS images, by aggregating QSCAT and ASCAT images to 8.9 km. The
120 resulting merged radar data set, named C-band Scatterometer (CScat), is publicly available in netcdf format at https://doi.org/10.6084/m9.figshare.20407857 (Tao et al., 2022a). Below, we provide a detailed illustration on the source data, methods, quality, and validation of the CScat data set.
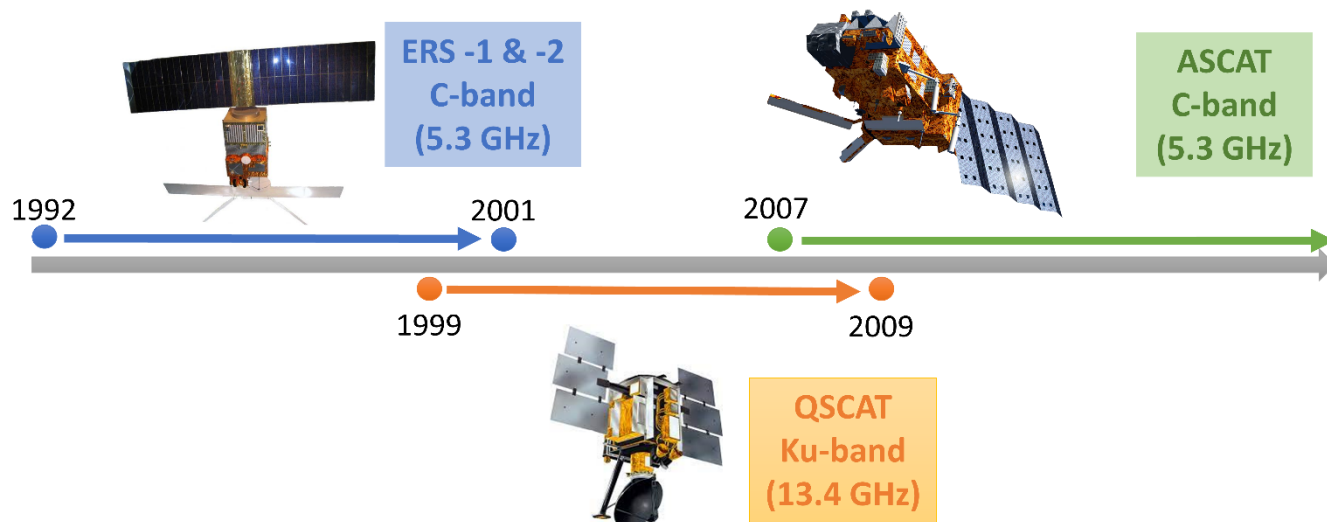
Figure 1. Temporal coverages and radio frequencies of ERS, QSCAT, and ASCAT. ERS and ASCAT have a C-band
radio frequency (5.3 GHz), and QSCAT have a Ku-band frequency (13.4 GHz). QSCAT operated between 1999 and 2009 in
full mode, overlapping with both ERS and ASCAT. Images of ERS, QSCAT, and ASCAT are also shown. Image Credit:
NASA, ESA and EUMETSAT.

2 Data and Methods

2.1 ERS, QSCAT, and ASCAT Data

Scatterometers were originally designed to measure wind speed and direction, particularly over oceans. However, their data
have also been found as useful for land applications such as soil moisture estimation, rainfall estimation, and forest monitoring.
Here we analyzed space-borne scatterometer data from the ERS, QSCAT, and ASCAT sensors (Fig. 1). The backscatter of the
radar signal, usually expressed in decibels (dB), is a function of the sensor parameters (frequency, polarization, look angle and
spatial resolution), and the dielectric and geometric properties of the scattering objects.

ERS-1, launched in 1991 by the European Space Agency (ESA), is the first spaceborne C-band scatterometer with repeated
and global geographical coverage. The ERS-1 mission ended on March, 2000 because of a failure of the attitude control system.
ERS-2 was then launched by ESA in April 1995 as a follow-up to ERS-1. However, starting from early 2001 until the end of
mission in 2011, ERS-2 has been operating without gyroscopes, which largely reduced its spatial coverage (Carabajal and
Harding, 2006). Consequently, the distribution of global coverage ERS-2 images to the user community was discontinued for
the period 2001-2011. Both sensors operate on a sun-synchronous near-circular polar orbit, passing the Equator at 10:30 am
in descending mode. The incidence angle of ERS-1 and ERS-2 ranges from 16 to 50 degrees. ERS-1/-2 images were acquired
in vertical (V-) polarization mode, and were usually gridded at 25 or 12.5 km resolutions (Frison and Mougin, 1996).

145 The SeaWinds scatterometer (13.4 GHz, Ku-band) onboard QSCAT was launched by NASA in 1999 and collected data in full mode until November 2009. It provides normalized cross-section backscatter values at fixed incidence angles of 46 degree in H- polarization mode and 54.1 degree in V- polarization mode. Its ascending and descending orbits cross the Equator at 6:00 am and 18: 00 pm local standard time, respectively. The QSCAT images are normally delivered at a resolution of 22 km × 22 km (Tsai et al., 2000).

150

 ASCAT, onboard the Meteorological Operational (Metop) series of satellites, was launched in October 2006 as a successor of the ERS-1/-2 scatterometers. The frequency of ASCAT (5.255 GHz, C-band) was designed to be consistent with ERS, although the range of its incidence angles was extended to cover 25—65 degrees. ASCAT passes the Equator at 9:30 am in descending mode and 21:30 pm in ascending mode. The backscatters of ASCAT are often grided at a spatial resolution of 25
155 km or 50 km. ASCAT images are available in V- polarization mode, as for ERS-1 and ERS-2 (Figa-Saldaña et al., 2002).

The NASA SCP project has enhanced the resolutions of ERS-1/-2, QSCAT, and ASCAT images to a nominal image pixel resolution of 8.9, 4.45, and 4.45 km/pixel, respectively. We downloaded the enhanced resolution images from the Brigham Young University (BYU) Center for Remote Sensing (www.scp.byu.edu/). The images are available for typical global regions
160 under the Lambert Equal Area projection, including Europe, Bering Sea, Siberia, North America, East Asia, Central America, Australia, Alaska, Oceania, North Africa, Southern Africa, South America, and South Asia. Three regions, namely Antarctica, Greenland, and the Arctic region, were not considered in this research because of the lack of QSCAT and ASCAT images in the BYU version. Images were provided in the 'SIR' format, which were read and displayed using the functions provided at https://www.scp.byu.edu/downloads.html.

165 **2.2 Data pre-processing**

We first aggregated QSCAT and ASCAT images of the BYU version at the resolution of ERS images, namely 8.9 km/pixel. Ascending path QSCAT and ASCAT images were used. The ascending path time of QSCAT acquisition (6:00 am) is before sun rise, and the ascending path time of ASCAT (21:30 pm) is well after sun set, both reflect nighttime land surface conditions. The ERS images of the BYU version are generated by combining images of all paths to ensure the highest possible spatial and
170 temporal coverages, we therefore used the all-path ERS-1/-2 images.

V-Polarization QSCAT images were merged with V-Polarization ERS and ASCAT images. H-Polarization QSCAT images were also tried but very similar merged signals were obtained. The BYU data center provides images synthesized from acquisitions made over periods of 17, three, and four consecutive days for ERS, QSCAT, and ASCAT respectively. For all
175 three sensors, images acquired within a month were averaged. ERS and ASCAT observations of the BYU version were normalized to a common 40-degree incidence angle to be free of angle influence on the observations. Monthly signals

exceeding three standard deviations from the long-term mean were consider to be outliers. Some ASCAT images were found to have strip patterns. Fortunately, all the strips were characterized by regions with a low number of radar observations, and thus can be masked by thresholding for a minimum number of observations, which was set to 20 (Tao et al., 2022b). To avoid

180   water contamination on the signal, we excluded pixels within which more than 2% of the pixel area are classified as "water" according to the 300-m resolution ESA Climate Change Initiative (CCI) land-cover map for the year 2015 (maps.elie.ucl.ac.be/CCI/viewer/).

2.3 Scaling radar time series

Similar to Tao et al. (2022b), a two-step approach was used to merge the C-band (ERS-1/-2 and ASCAT) and Ku-band

185   (QSCAT) signals into a continuous long-term radar data set. The first step of the method was to unify the backscatter values from different sensors (i.e., data rescaling). The second step was to harmonise the scaled data into a smooth time series by addressing their monthly differences (Fig. 2).
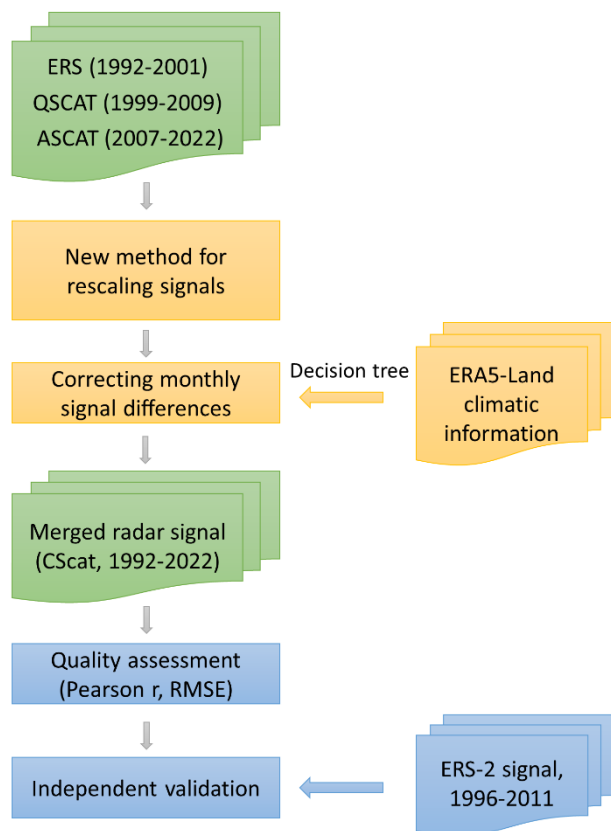
Figure 2. Flow chart illustrating the development and assessment of the CScat data set. Inputs/outputs are colored in green, the signal merging procedures colored in yellow, and assessment and validation for the merged signals colored in blue.

Regarding data rescaling, previous testbeds have proposed two methods for rescaling time series: a linear regression correction (Brocca et al., 2011), and a cumulative density function (CDF) matching technique (Liu et al., 2009). The linear regression correction involves first scaling a time series within the range of the reference time series, and then applying a linear regression equation between the two to minimise error. The CDF method further divides two time series into their quantile segments, and then constructs a regression for each segment so that the CDF of a time series matches the CDF of the reference time series (Liu et al., 2009).

However, we found that the CDF method failed in regions with a strong QSCAT signal trend such as the deforested areas in southern Amazonia (Fig. 3a). This is mainly because QSCAT and ASCAT overlapped during three years, and the QSCAT signals in these three years do not cover the full signal range during 1999 - 2009. Linear regression correction, as used in Tao et al. (2022b), is a preferable option to cope with this issue (see Fig. S1), but it is sensitive to sudden changes in radar signal (Fig. 3b). To overcome these limitations, we designed a new data rescaling method, illustrated in the following equation:

$$Q_{scaled} = (Q_{original} - Q_{mean\_overlap}) / Q_{std\_overlap} * A_{std\_overlap} + A_{mean\_overlap} \quad \text{(Eq. 1)}$$

where Q_{scaled} indicates the scaled QSCAT signals, and $Q_{original}$ means the original QSCAT signals prior to signal rescaling. $Q_{mean\_overlap}$ and $Q_{std\_overlap}$ indicate the mean and standardized deviation of the QSCAT signals with ASCAT in the overlapping period (i.e., 2007-2009). Likewise, $A_{mean\_overlap}$ and $A_{std\_overlap}$ indicate the mean and standardized deviation of the ASCAT signals in the overlapping period. This method was found to be robust to both the trends and sudden changes in radar signal (Fig. 3). We therefore used it to unify the scales of ERS, QSCAT and ASCAT signals. Specifically, monthly QSCAT signals were first scaled against monthly ASCAT signals, pixel by pixel. We chose ASCAT as the baseline for the rescaling because it has the best radiometric quality (lower sensitivity, higher radiometric resolution), and because it is still operational. Thereafter, ERS signals were scaled against QSCAT signals (already scaled against ASCAT) using the same method. The ERS-1 and ERS-2 data sets were already calibrated, so there was no need to rescale them separately.
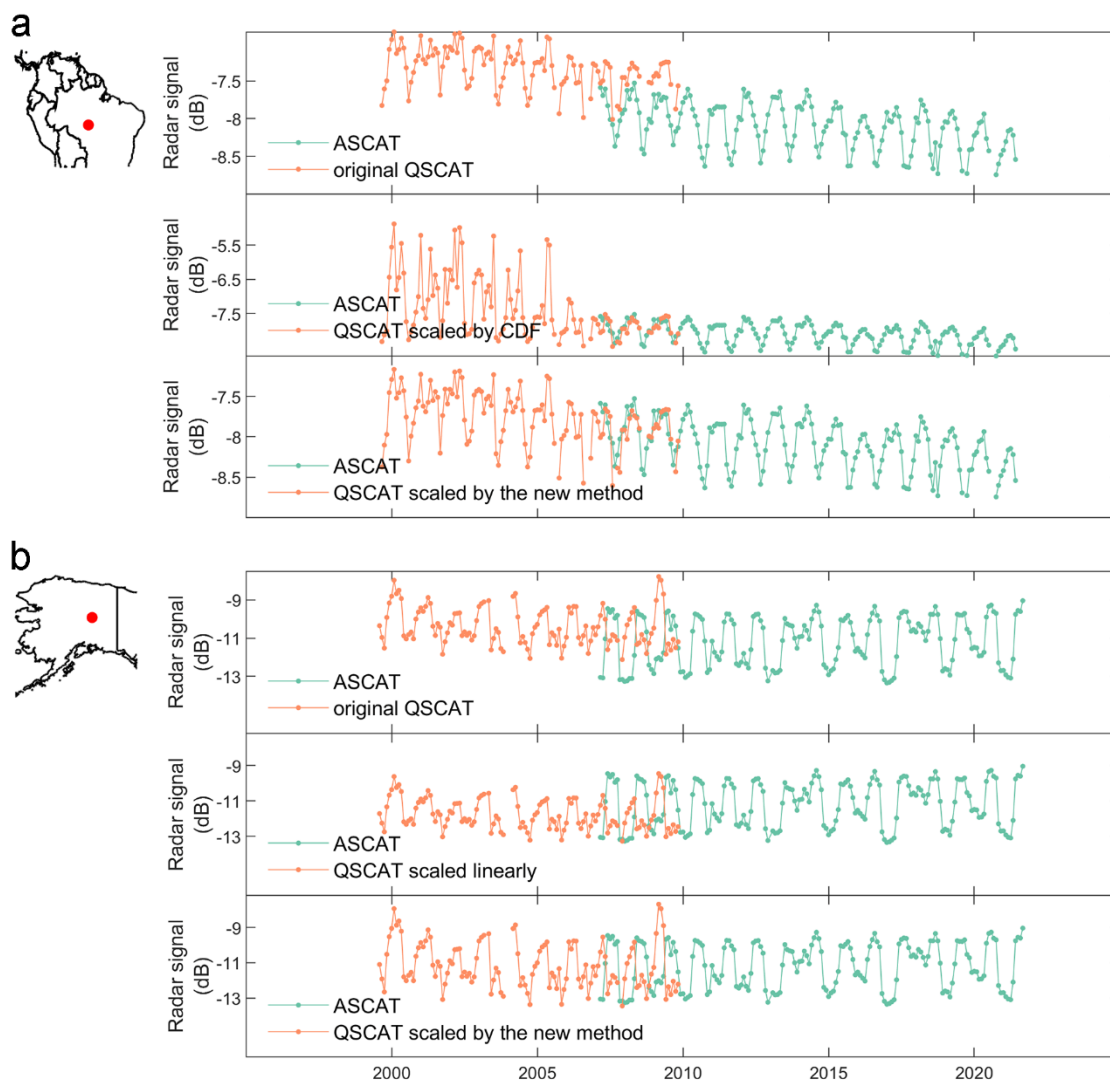
Figure 3. Comparisons between the CDF method, the linear regression correction, and the new method for rescaling radar signals. (**a**) Comparison between the new method and the CDF method for rescaling a QSCAT signal time series with a strong decreasing trend. (**b**) Comparison between the new method and the linear regression correction for rescaling a QSCAT signal time series with sudden increases during the overlapping period.

2.4 Addressing the monthly signal differences

We seek here to correct the monthly signal differences before averaging the scaled signals. Indeed, previous research averaged directly the scaled signals to obtain a single merged time series (Du et al., 2017; Moesinger et al., 2020). We found large monthly signal differences between the C-band and the scaled Ku-band signals in tropical regions. Importantly, the differences

showed a seasonal pattern, with the Ku-band radar signal higher than C-band signal during the dry season, and lower in the
230   wet season. Thus, we attempted to model the signal differences using rainfall as a predictor (Fig. 4a; Weissman et al., 2012;
Prigent et al., 2022). The effects of rainfall could be explained by the fact that the Ku-band signal has a short wavelength and
low penetrating ability relative to C-band, thus is more affected than the C-band signal by tropical rainfall and water intercepted
at the top of the forest canopy (Tao et al., 2022b).
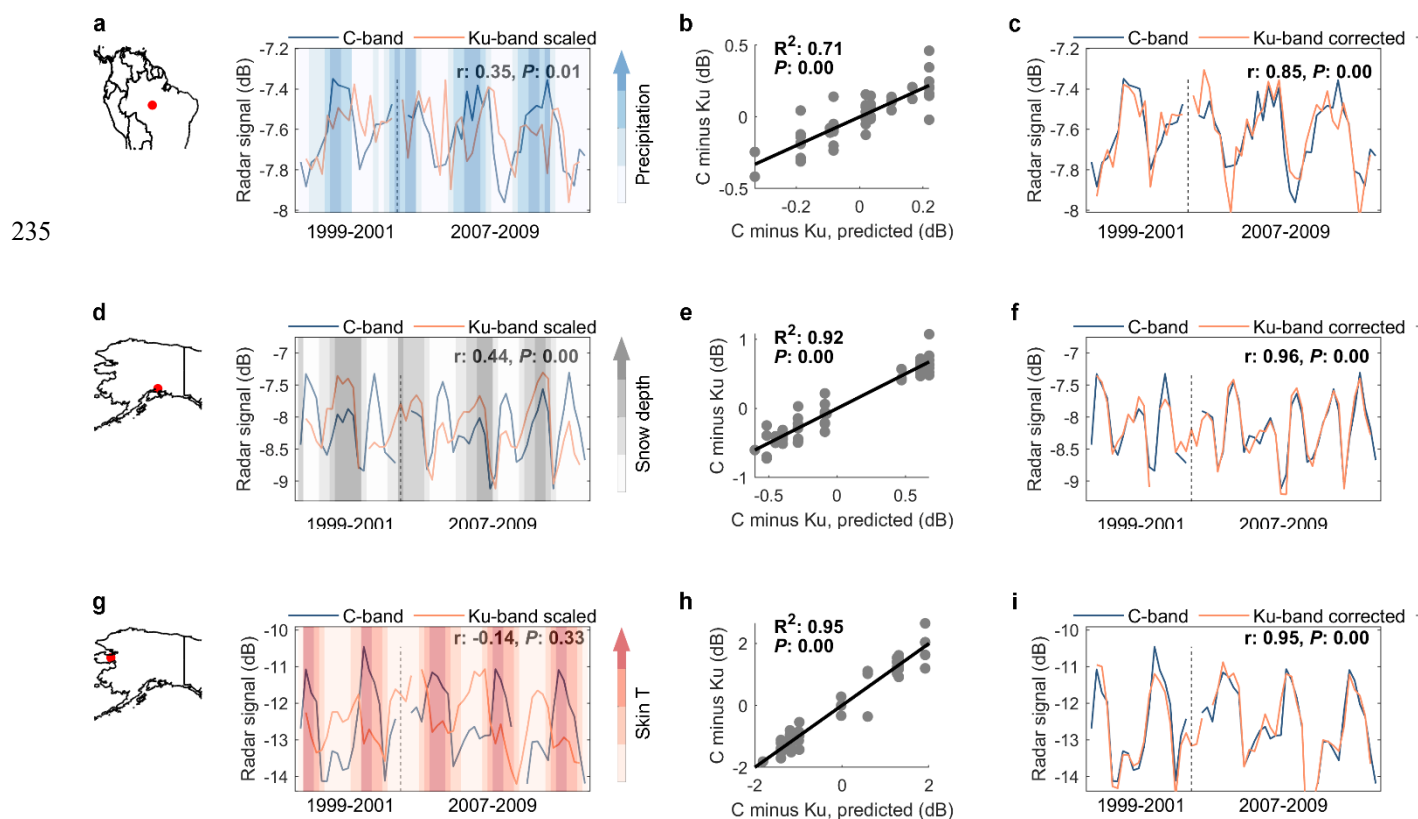
240

**Figure 4. Illustration on the correction of the monthly signal differences between the C-band and the scaled Ku-band
signals in the overlapping years (1999-2001 and 2007-2009).** (**a**) The C-band and the scaled Ku-band signals before
correction in one pixel of Amazonia. The location of the pixel is indicated by a red dot in the left-most map. The blue-white
background shows the monthly precipitations. (**b**) Predicted signal differences by decision tree regression with precipitation
245   as input *versus* observed signal differences. (**c**) The C-band and the corrected Ku-band signals. The vertical dotted line in **a**
and **c** separates the ERS-QSCAT overlapping (1999–2001) and QSCAT-ASCAT (2007–2009) overlapping periods. (**d-f**) show
one example of the signal correction in Alaska with snow depth as the predictor of the signal differences. (**g-i**) show one
example of the signal correction in Alaska with skin temperature as the predictor of the signal differences.

To extend our previous approach to the global scale, we explored the monthly signal differences against not only rainfall but
250   also snow depth and skin temperature, for the following reasons:

1. Analogous to the effect of rainfall on Ku-band signals in tropical regions, we expect that snowpack prevents the
Ku-band signal from reaching the land surface in regions covered by snow (Kelly et al., 2003; Naeimi et al., 2012). Our
analysis in Alaska confirmed this point: Ku-band signals closely track the seasonal changes in snow depth derived from the
ERA5-Land archive (0.1 x 0.1 degree resolution, Muñoz-Sabater, 2019) (Fig. 4d-f).

255   2. Skin temperature is correlated with snow depth and rainfall amount. In addition, skin temperature is related with a
range of ecological or hydrological processes such as surface freeze/thaw in cold regions. One example is shown in Fig. 4g-i:
monthly mean skin temperature (also from the ERA5-Land archive) predicts the signal differences in the western Alaska where
permafrost is present. We therefore also expect that skin temperature is an effective predictor of the signal differences.

Based on this prior knowledge, the following steps were designed to correct the monthly signal differences on a global
260   scale:

1.   For each pixel, the monthly signal differences during the overlapping periods (i.e., 1999-2001, and 2007-2009)
were regressed, separately, against monthly rainfall, snow depth, and skin temperature derived from the
reanalysis ERA5-Land archive. Decision tree regression (Sankaran et al., 2005) was used because the
relationships between signal differences and climatic variables could be non-linear.

265   2.   Signal differences during the overlapping periods were then predicted by the regressions established in step 1,
and added back to the scaled Ku-band signals. As a result, we obtained three sets of corrected Ku-band signals
in the overlapping periods. Pearson r values between the C-band signals (also from the overlapping periods) and
each of the three sets of corrected Ku-band signals were then calculated. The Pearson r value was used to judge
which regression (or which climatic variable) most accurately predicted the signal differences. We verified that
270   the quality of the final merged signals was unaltered if mean squared deviation (MSD, Kobayashi and Salam,
2000) rather than Pearson r was used to select the optimal regression.

3.   The optimal regression selected in step 2, established with data from the overlapping periods, was applied on
climatic data from 1999 to 2009, and the predicted signal differences were added to the full QSCAT time series.
The data merging procedure was applied pixel by pixel. After transforming the QSCAT data, we built a time
275   series for each pixel for the 1992–2022 period, averaging data from the overlapping periods (1999–2001 and
2007–2009). To assess the effectiveness of the data merging approach, Pearson r, RMSE, and relative RMSE
(rRMSE) between the C-band and the corrected Ku-band signals in the overlapping periods (1999-2001 and
2007-2009) were finally calculated.

280
$$r = \frac{\sum(x_i - \bar{x})(x_i - \bar{y})}{\sqrt{\sum(x_i - \bar{x})^2 \sum(y_i - \bar{y})^2}} \qquad (2)$$

$$RMSE = \sqrt{\frac{\sum(x_i - y_i)^2}{n}} \qquad (3)$$

$$rRMSE = \frac{RMSE}{\sigma_y} \tag{4}$$

where $\bar{x}$ denotes the mean of the monthly Ku-band signals x in the overlapping years; $\bar{y}$ denotes the mean of the monthly C-
285   band signals y in the overlapping years; x_i and y_i denote the values of x and y at the i-th month, respectively; σ_y denotes the

standard deviation of y; and n denotes the number of months in the overlapping years. rRMSE was used because it is

normalized against the standard deviation of the signal, thus can be compared across regions.

2.5 Validation of the data merging approach

We also conducted a stricter evaluation of the data merging approach. From January 2001 to 2011, the ERS-2 satellite
290   experienced a series of failures that affected its data continuity and spatial coverage. However, observations were occasionally

available for a subset of global pixels (Crapolicchio et al., 2012). This period overlaps with the QSCAT operating period, thus

it can be used to test whether the corrected Ku-band (QSCAT) signal shows consistent dynamic with the C-band signal.

Recently, the European Space Agency (ESA) has released the ERS-2 data set for the period of 2001–2011 (Crapolicchio et al.,

2012). We used this version of ERS-2 data (hereafter referred to as ESA ERS-2) to validate our data merging approach.
295   Excluding Australia, Southern Africa, and the Bering Sea, ten out of the 13 global regions were covered by the ESA ERS-2

data set during 2001 and 2011. For each of these ten regions, we calculated monthly radar backscatter coefficients at 40-degree

incidence angle from the ESA ERS-2 data set, for comparison with our merged radar data set. To normalize the incidence

angle, a linear regression was fitted between all incidence angles and the radar backscatter coefficients, and the R squared

value and RMSE value of the regression were reported. The backscatter coefficient at 40-degree incidence angle was then
300   predicted by the regression. To ensure data quality, the predicted backscatter coefficient was not used if the RMSE was higher

than 0.5. Since the ESA ERS-2 data have a resolution of 25 km, we aggregated our merged radar signals to that resolution. For

each month during 2001 and 2011, pixels with available ESA ERS-2 observations were located, and their ERS-2 signals were

averaged across pixels. Because the footprints of the ESA ERS-2 observations are not fixed temporally, different months have

different subset of pixels. Our merged radar time series from the same pixels were then averaged and compared with the ESA
305   ERS-2 signal mean. Months with too few pixels (<100) having ESA ERS-2 observations were not considered. This increases

the strictness of the comparison in the sense that there is an additional spatial variation of pixels embedded within the radar

time series.

3 Results

3.1 Merged radar signals and quality assessments

310   The merged radar signal, averaged across pixels within a region, is presented in Fig. 5. Pearson r, RMSE and rRMSE between

the C-band and the corrected Ku-band signals in the overlapping years (1999-2001 and 2007-2009) were used to assess the

quality of the merged radar signal. All 13 regions had a r value larger than 0.93, with a maximum of 0.99. We also obtained low RMSE values (from 0.03 to 0.16), even in regions with a large seasonal amplitude in radar signal, such as Siberia where the seasonal amplitude is around 3 dB but the RMSE is only 0.16. This result was further confirmed by the low rRMSE values

315 obtained in all regions, which ranged from 0.09 to 0.37.
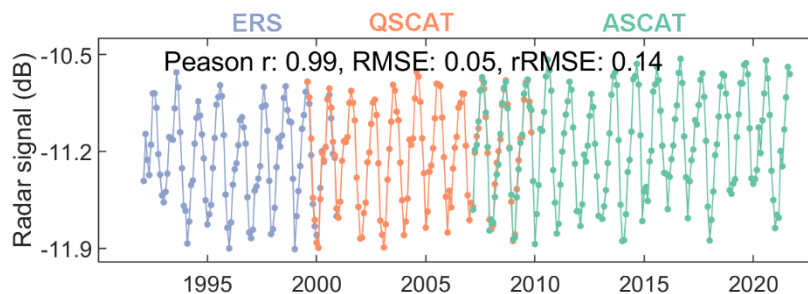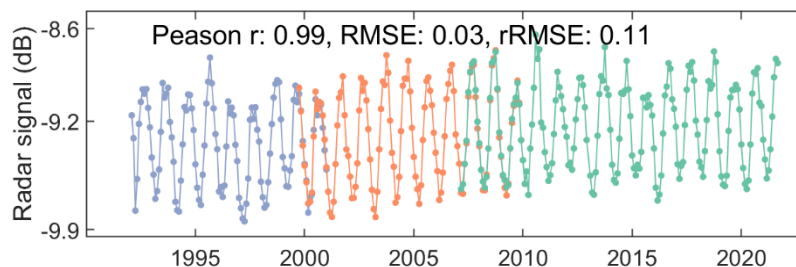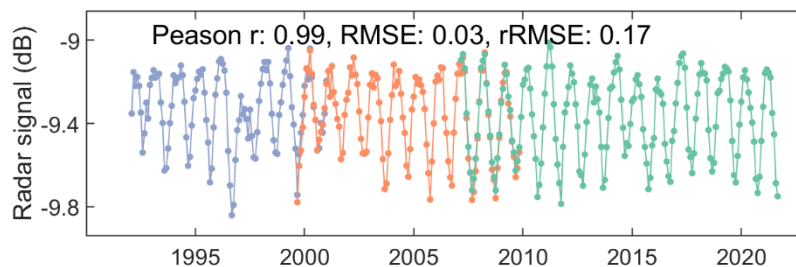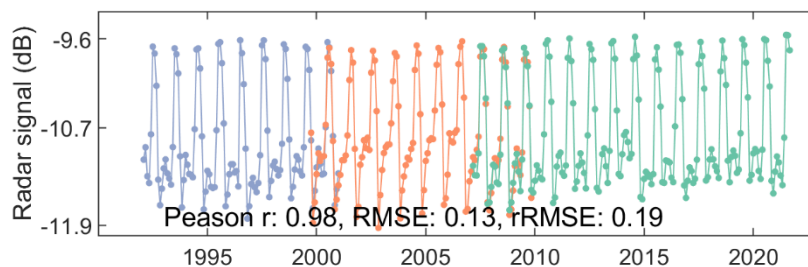
320

Alaska
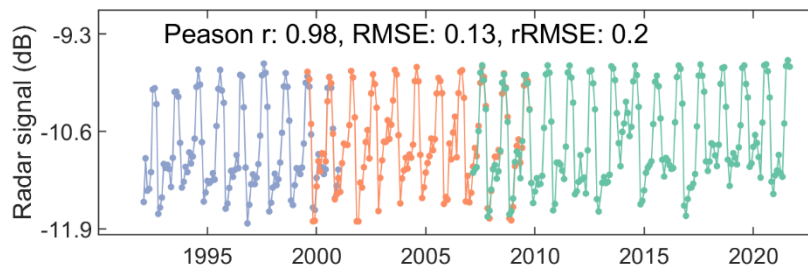
Europe
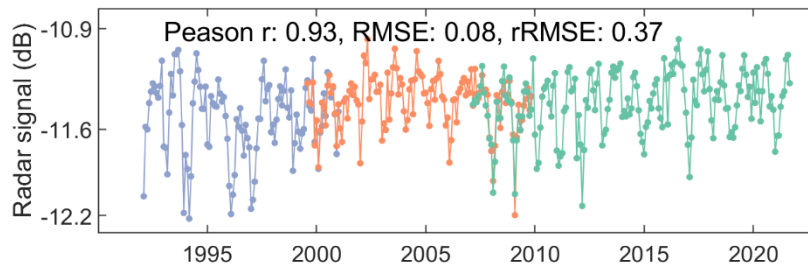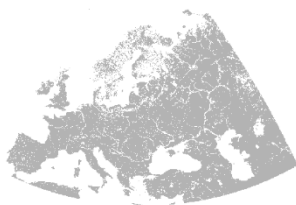
North Africa

Southern Africa

325

330
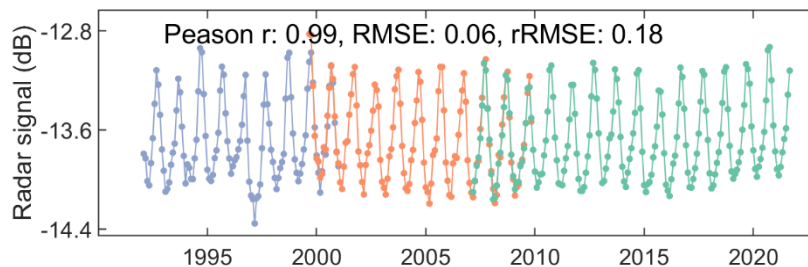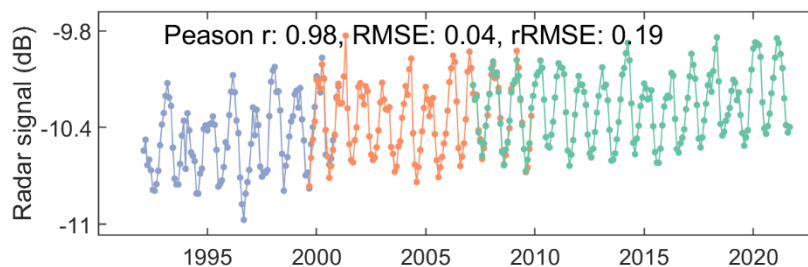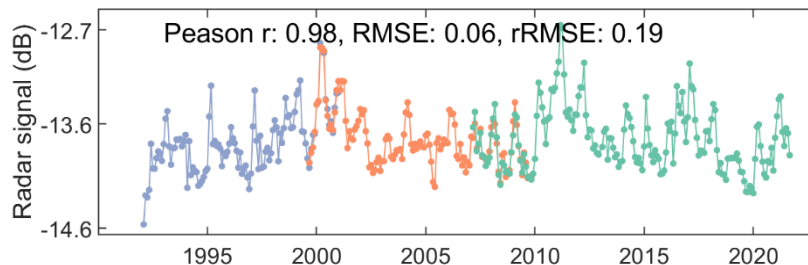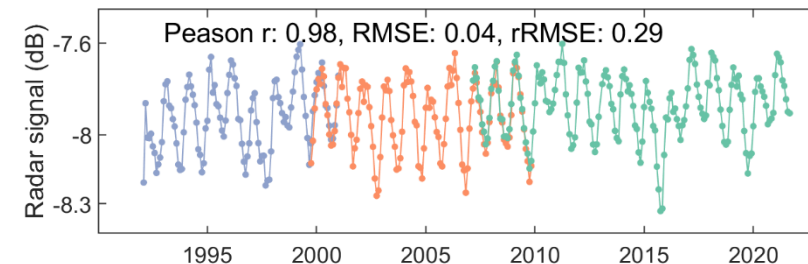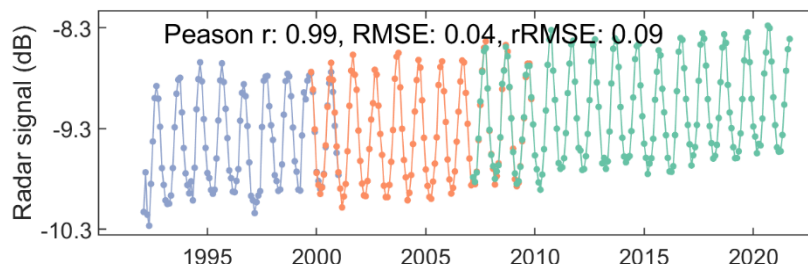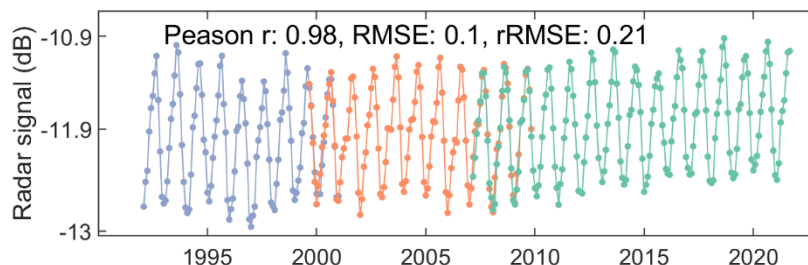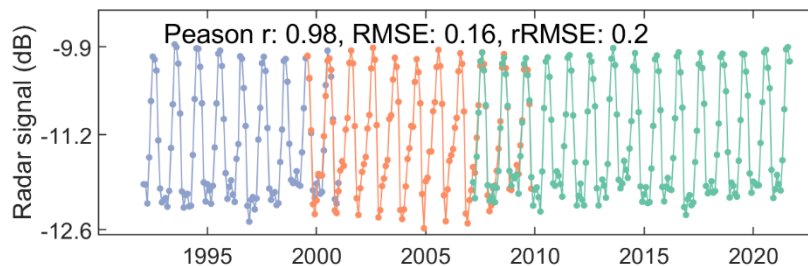
Figure 5. Time series and quality assessment of the merged CScat radar time series. Each row shows one region. Inside each row, the map in the left panel shows the location of the region. Lambert equal area projection is used in the map. The line plot in the right panel shows the merged radar time series colored according to sensors. The Pearson r, RMSE and rRMSE labelled in the panel were calculated using the C-band and the corrected Ku-band signals in the overlapping years (1999-2001 and 2007-2009), as indicators of the data merging quality.

We further assessed the data merging quality at the pixel level. Before correcting the monthly signal differences, the Pearson r values between the C-band and the scaled Ku-band signals showed a long-tailed distribution in all regions (Fig. 6). Regional median r values were relatively low, ranging from -0.22 to 0.91, and negative r values were found in almost all regions. After correcting the monthly signal differences, the regional median r values ranged from 0.80 to 0.96, with no negative r values observed (Fig. 6). The improvement was the most obvious in the northern high latitudes, such as Europe (r improved from 0.54 to 0.90), Bering Sea (r from -0.13 to 0.93), and Siberia (r from -0.22 to 0.93). In contrast, the improvements for five regions, namely Central America, Australia, North Africa, South America, and South Asia, were relatively limited, because their median r values prior to signal correction were already high. All five regions contain large portions of barren lands, deserts, shrublands, or grasslands, where the Ku-band signal is not as impacted as in forested and snow-covered regions.
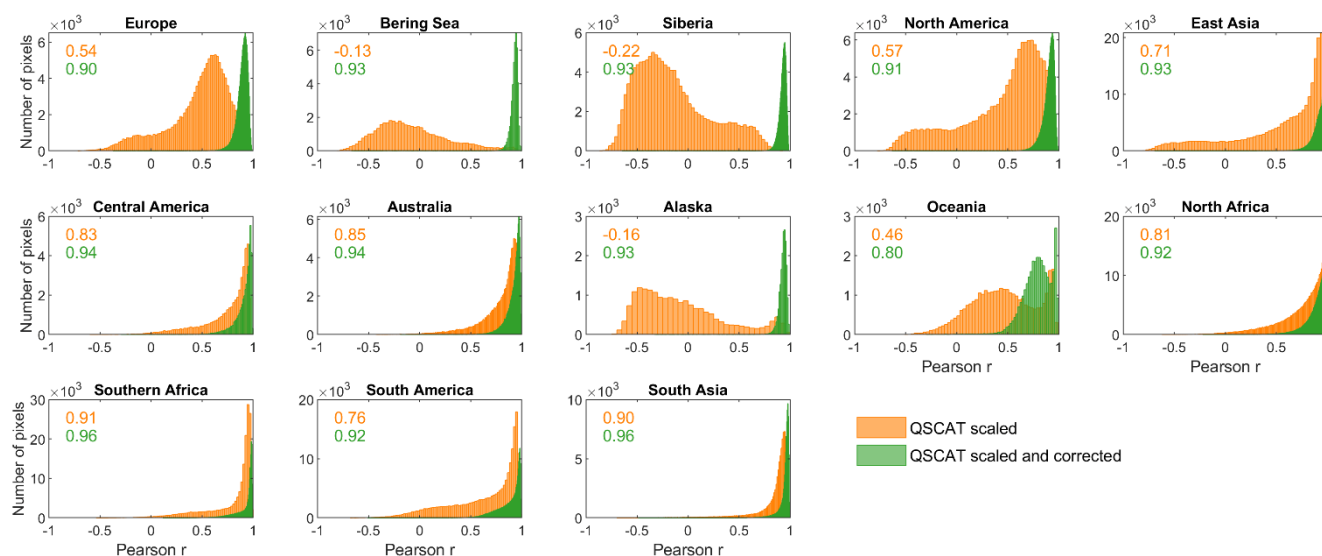
Figure 6. Pearson r-based quality assessment of the CScat data set at the pixel level. Each panel shows the result of one region. Inside each panel, the Pearson r values between the C-band and the scaled Ku-band signals in the overlapping years (1999-2001 and 2007-2009) were calculated for all the pixels in this region and colored in orange. As a comparison, the Pearson r values between the C-band and the corrected Ku-band signals in the overlapping years were also calculated and colored in green. The medians of the Pearson r values are labelled inside each panel.

Regarding RMSE (Fig. 7), regional median RMSE values varied between 0.15 and 1.52 before correction for signal differences, but decreased sharply after correction for signal differences (between 0.10 and 0.38; Fig. 7). The most obvious
360 improvement was still observed in the northern high latitudes such as Europe (RMSE decreased from 0.66 to 0.29), Bering Sea (RMSE from 1.32 to 0.33), and Siberia (RMSE from 1.52 to 0.38). Regional median rRMSE values were lower than 0.64, consistent with RMSE-based assessments (Fig. S2). Besides, in the final CScat data set, tropical regions, mountainous regions, and arid regions had relatively higher rRMSE values than other regions (Fig. S3).
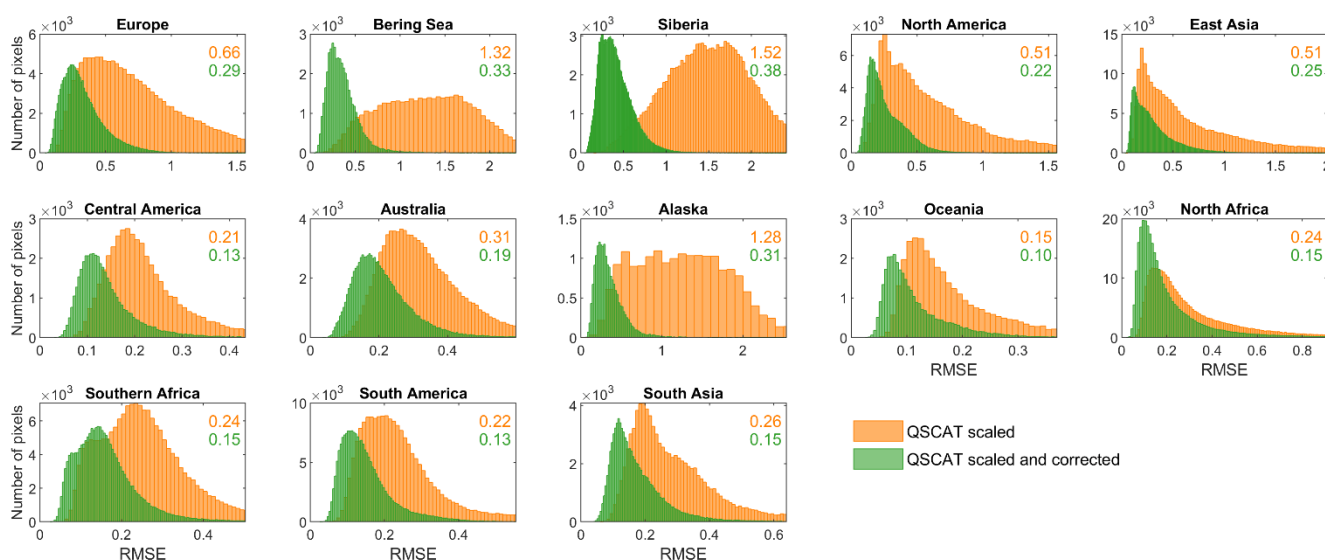
365

Figure 7. RMSE-based quality assessment of the CScat data set at the pixel level. Each panel shows the result of one region. Inside each panel, the RMSE values between the C-band and the scaled Ku-band signals in the overlapping years (1999-2001 and 2007-2009) were calculated for all the pixels in this region and colored in orange. As a comparison, the
370 RMSE values between the C-band and the corrected Ku-band signals in the overlapping years were also calculated and colored in green. The medians of the RMSE values are labelled inside each panel. rRMSE-based quality assessments are shown in supplementary material.

3.2 Importance of the predictor variables

375 For each pixel, we built three regression models including rainfall, skin temperature, and snow depth, respectively, as a predictor of the signal difference in the overlapping years (1999-2001 and 2007-2009). The climatic variable that most accurately predicted the signal differences was finally used for that pixel (see Section 2.4).

We found that, for 31% of all the pixels, signal differences were most accurately predicted by rainfall (hereafter referred to as
380 Type 1 pixels, Fig. 8a). This type of pixels was mainly found in the southern hemisphere, particularly in tropical regions. In the northern hemisphere, such pixels were primarily located in the low and middle latitudes (Fig. 8a).
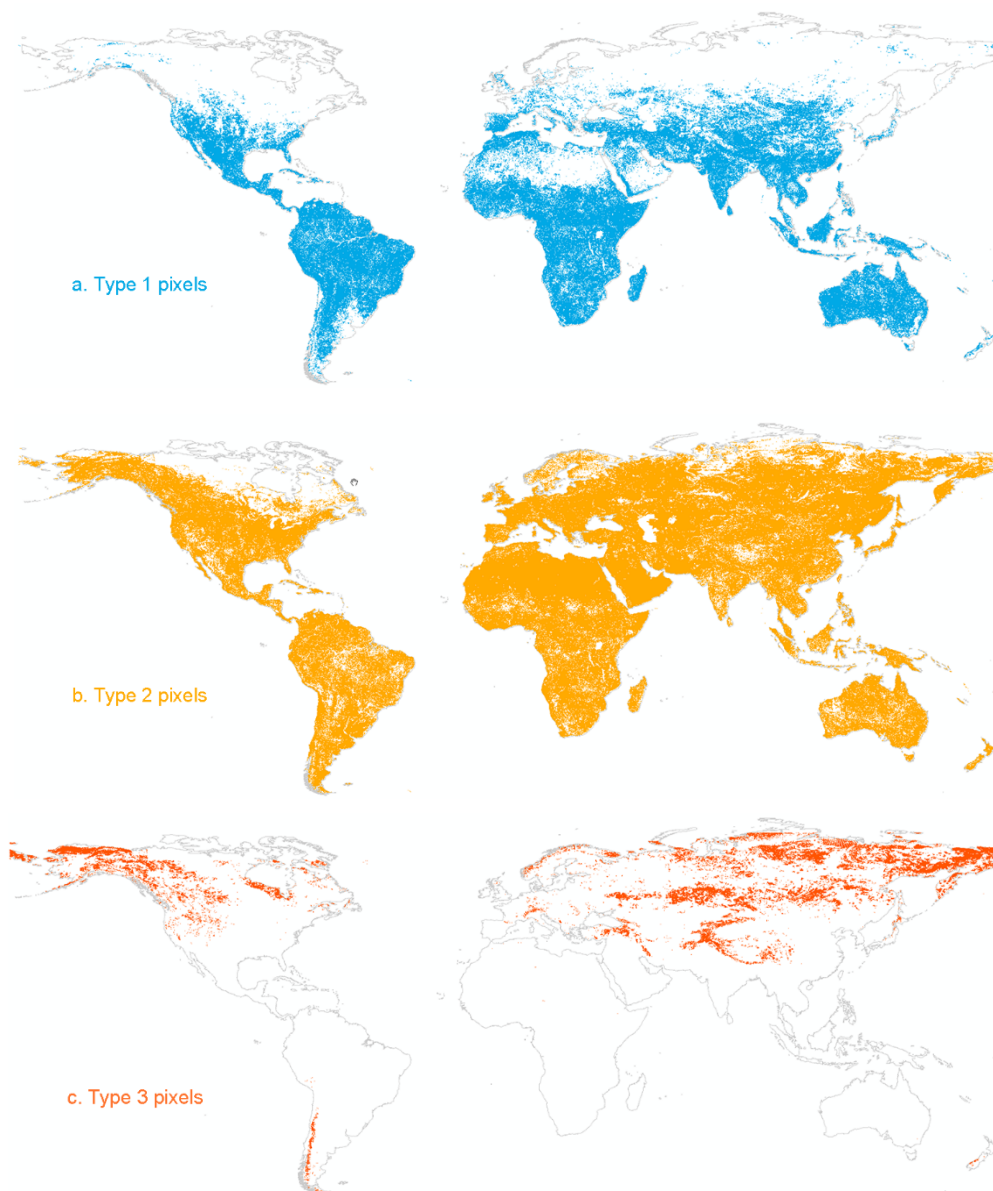
385

Figure 8. Spatial distributions of the different types of radar pixels. For Types 1, 2, and 3 pixels, the signal differences between the C-band and the scaled Ku-band signals in the overlapping years (1999-2001, 2007-2009) were most accurately predicted by monthly precipitation, skin temperature, and snow depth, respectively.

390   For 64% of all the pixels, signal differences were most accurately predicted by skin temperature (hereafter referred to as Type 2 pixels, Fig. 8b). This type of pixels was widely distributed across the globe. In tropical regions, the spatial pattern of Type 2 pixels is similar to the pattern of Type 1 pixels (Fig. 8a & 8b), which is expected because skin temperature and rainfall are correlated. The main differences between the distributions of Type 1 and Type 2 pixels were found in the northern high latitudes and dry regions such as the hyper-arid Sahara Desert.

395

Signal differences in the remaining 5% pixels were most accurately predicted by snow depth (Fig. 8c, hereafter referred to as Type 3 pixels). As expected, this type of pixels was primarily found in mountainous regions such as the Himalayas and the southern part of the Andes, as well as the very high-latitude regions in the northern hemisphere.

400   **3.3 Independent validation of the merged radar signal**

The quality of the merged radar signals was also validated directly against the ESA ERS-2 data (see Section 2.5). The number of ESA ERS-2 pixels available for a comparison differed across regions. Furthermore, the pixel number decreased largely around 2003 in many regions (Fig. S4). Despite the variations in pixel number, we found similar monthly dynamics between the merged radar signals and the ESA ERS-2 signals in all regions. Using the Pearson r value as an index of similarity, all

405   regions had a Pearson r value higher than 0.79, with a maximum of 0.98. Seven regions had a r value higher than 0.90 (ranging from 0.90 to 0.98) (Fig. 9). This validation evidences that the CScat data are unlikely to be biased due to the cross-period merging method.
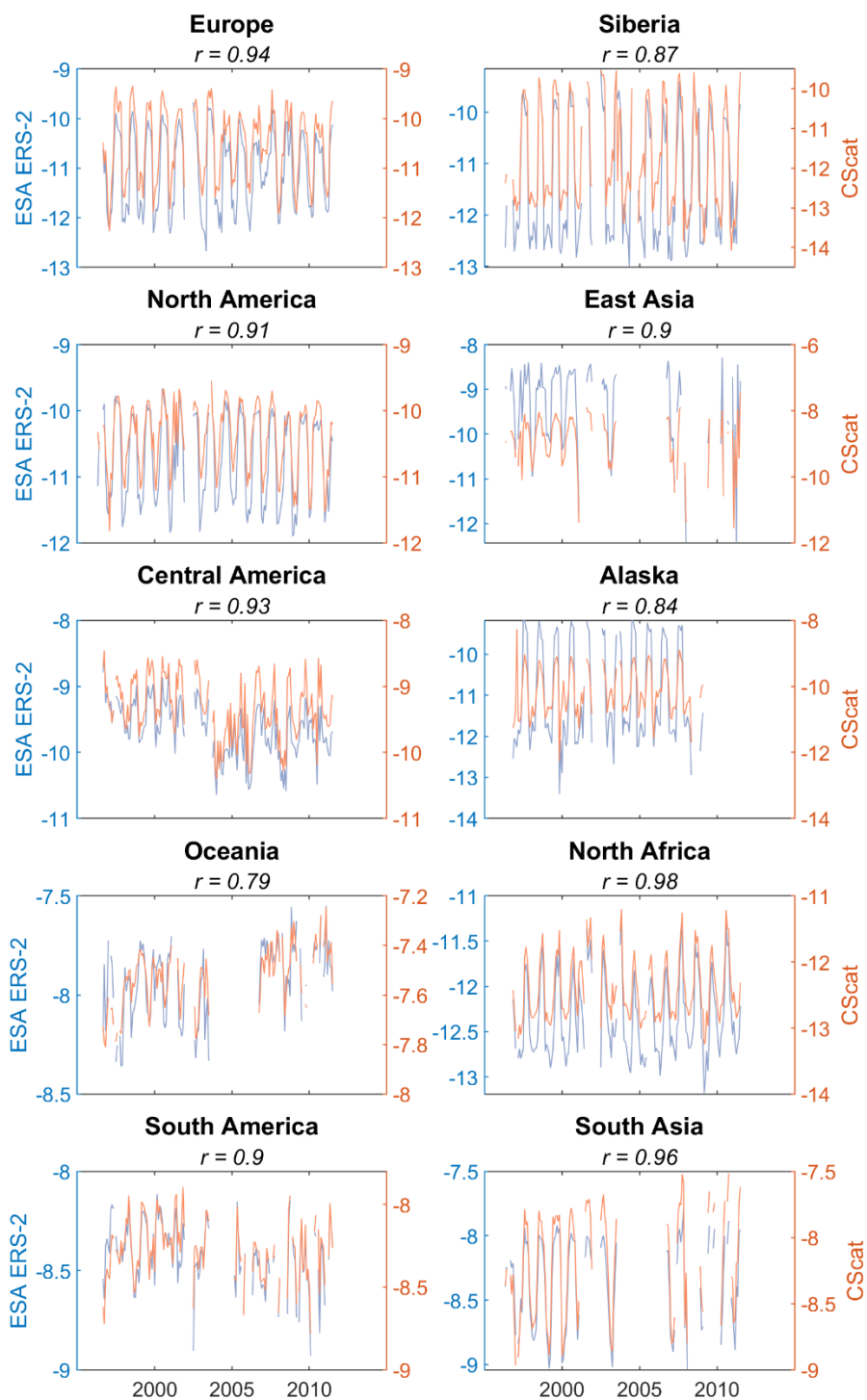
Figure 9. Validation of the merged CScat radar signals against the ESA ERS-2 data. The unit of signals is dB.

4 Discussion

4.1 New method for rescaling the radar time series

The purpose of this project was to create the first global long-term radar backscatter data set with a consistent C-band signal dynamic. C-band ERS (1992-2001) and ASCAT (2007-onwards) signals were bridged by Ku-band QSCAT (1999-2009) signals. Observations overlapped between the three sensors, which allowed us to rescale the signal times series.

The CDF matching technique has been a classical signal rescaling method (Liu et al., 2009; Liu et al., 2011; Liu et al., 2015). For instance, Liu et al. (2011) used the CDF method for recalling vegetation optical depth (VOD) derived from the Special Sensor Microwave Imager (SSM/I, 1987–2007), TRMM Microwave Imager (TMI, 1998–2008) and AMSR-E (2002–2008) sensors. Moesinger et al. (2020) also used it for rescaling VOD products from SSM/I, AMSR-E, AMSR2 (2012-2019), and WindSat (2003-2012). In these previous studies, the overlapping periods among sensors are relatively long, some even exceeding ten years. In contrast, neither the ERS-QSCAT nor the QSCAT-ASCAT overlapping periods span more than three years. The rescaled QSCAT signals by CDF could therefore be biased, due for instance to deforestation in southern Amazonia (Fig. 3a). The linear regression correction can tackle this issue (Fig. S1, Tao et al. 2022b), but is sensitive to sudden changes in radar signal. As shown in Fig. 3b, the QSCAT signal surged in 2009 in one location of Alaska, and the linear regression correction created an obvious bias in the rescaled QSCAT signals. This situation is rare in tropical regions but appears more frequent in northern high latitudes, due to the surface freeze/thaw process. Although we have excluded potential outliers from the radar signals by implementing a standard deviation filter (see Section 2.2), such sudden changes were not identified as outliers.

Our new method for rescaling the signal time series (Eq. 1) is rooted in the discipline of statistics, and all the terms shown in Eq. 1 have been frequently used in physical and social sciences. However, as far as we know, this is the first time such a rescaling of microwave signals is performed with a short overlapping period. The results shown in Fig. 3 suggest that this method is robust to both the trends and sudden changes in radar signal. Thus, it could be considered by future research for merging signal times series with limited overlapping observations.

4.2 Signal quality and merging mechanism

After rescaling the radar time series from different sensors, monthly signal differences were corrected, by modelling them from climatic variables (namely precipitation, skin temperature, and snow depth). The quality of the merged radar signals was assessed against the ESA ERS-2 data set. Highly similar monthly time series were obtained, suggesting high accuracy for the merging procedure.

Why did rainfall, skin temperature, and snow depth successfully predict the signal differences? The main reason is that the Ku-band signal has a lower penetrating ability in comparison to the C-band signal because of its shorter wavelength. In regions with a strong rainfall such as the tropics, Ku-band signals are more impacted by raindrops and the intercepted water on forest top-canopy, thus showing different seasonal patterns with C-band signals (Fig. 4a). The rainfall attenuation of high frequency microwave signals (Ku/Ka band or 13/35 GHz) is used for microwave-derived rain retrieval, such as the case of precipitation radar operating at 13.8 GHz on board TRMM (Iguchi et al., 2000).

Skin temperature is found to be the most effective predictor of the signal differences for almost two thirds (64%) of all the pixels (Fig. 8). This is expected because skin temperature not only corelates with rainfall, but also reflects several land surface processes. In tropical regions, skin temperature was found as an almost equally important predictor of signal difference as rainfall. The first explanation for this result is that there is a negative correlation between skin temperature and rainfall in tropical regions (Fig. S5). A second explanation could be the increased evapotranspiration of the rainforest canopy in dry periods due to high vapor pressure deficit. Increased evapotranspiration is correlated with skin temperature, and could impact the Ku-band signals, influencing top canopy moisture. This phenomenon therefore helps explain why Ku-band signals are higher than C-band signals in dry periods (Guan et al., 2015; Konings et al., 2017).

In boreal regions (Fig. 8b), skin temperature is also the most effective predictor of the signal differences. This could be related with the fact that the local land surfaces in these regions are seasonally frozen, or covered by ice, causing different signal performances between Ku-band and C-band signals. The surface freeze/thaw cycle is reflected by skin temperature changes, explaining why skin temperature predicted signal difference in these regions.

In arid regions such as central Austria, the Sahara Desert and the Arabian Desert (Fig. 8b), skin temperature also outperformed rainfall as a better predictor of the signal differences. These regions receive limited amount of rainfall annually. Soil moisture is therefore mainly controlled by land surface processes, such as the seasonal changes in wind intensity and direction in deserts which modify the roughness of the sand dunes and finally lead to a temporal variation in soil moisture (Frédéric et al., 2015). Soil moisture changes with skin temperature, leading to changes in the penetration depths of C-band and Ku-band signals, due to the attenuation of the microwave signal as a function of moisture. This hypothesis could explain why skin temperature is closely related with the signal differences in some arid regions.

Snow depth was found to be the most effective predictor of the signal differences in mountainous and high-latitude regions seasonally covered by snow. The Ku-band signal interacts with snows because of its short wavelength, thus its dynamics follows the seasonal changes in snow depth. Ku-band signal is higher when snow depth is deeper and vice versa (Fig. 4d), but C-band signal shows the opposite dynamics, possibly because of a deeper penetration. We therefore modelled the signal differences using snow depth as a predictor. In fact, this is a reversed version of the classical approach which models snow

depth or snow-water equivalent from microwave signal differences (Kelly et al., 2003). Since the launch of Scanning Multichannel Microwave Radiometer (SMMR) in 1978, microwave data have been used to estimate snow depth and snow-water equivalent. One of the classical methods is based on the fact that microwaves at different frequencies respond differently to snow cover. For instance, the Chang equation (Chang et al., 1982) utilizes the channel differences between low- (such as 19

480 GHz) and high- (such as 37 GHz) frequency brightness temperatures observed by passive microwave sensors. Here, we found similar signal differences between low- (C-band) and high- (Ku-band) frequency radar signals. Since several radar sensors at different frequencies are operating, efforts could be made to create products of snow depth or snow-water equivalent based on radar sensors such as QSCAT and ASCAT.

485 Although we calculated, for each pixel, the most effective climatic variable for predicting the signal differences, this does not necessarily mean that the signal differences are explained by a single climatic variable. In many cases, precipitation, snow depth, and skin temperature indicate three phases of the same climatic or hydrological process, such as the rainfall-snow/ice formation- snow/ice melt cycle in the Tibetan Plateau and Alaska. This is evidenced by the fact that all three variables predict the signal differences with high accuracies in the Tibetan Plateau (Fig. S6). It is also worth noting that, although climatic data

490 were used to merge radar signals into a single time series, this does not mean our final radar signals contain mainly climate information. The three climatic variables were merely used to model signal differences, which were then added to the Ku-band signals. Besides, the 1999-2009 period accounts for only a third of the entire time span. Thus, the main information contained in the merged signals is related to features of the land surface rather than to climate.

495 4.3 Limitations and future works

We used the reanalysis ERA5-Land monthly climatic data to model the signal differences. As a result, whether signal differences can be accurately modelled partly depends on the accuracy of the ERA5-Land climatic data. Future work will test the effectiveness of other climatic data sets for modelling the signal differences. The accurate mapping of some climatic variables, such as snow depth, are challenging (Orsolini et al., 2019; Clifford, 2010; Pulliainen et al., 2020). This is critical in

500 the high-latitude regions such as northern Alaska, where snow depth is the most important variable predicting the signal differences. The estimation of rainfall is also challenging in regions with sparse climate stations such as the tropics. An increasing amount of climate data sets has been made publicly available, including the Modern-Era Retrospective analysis for Research and Applications Version 2 (MERRA-2, Gelaro et al., 2017), and the Climate Hazards Group InfraRed Precipitation with Station data (CHIRPS). The snow depth product of MERRA-2 has been demonstrated as superior than ERA5 in mainland

505 China (Zhang et al., 2021). The CHIRPS precipitation was also validated to have an excellent performance in tropical Africa (Camberlin et al., 2019). Thus, it is possible that these climate products may produce a better merging quality for tropical and mountainous regions where the rRMSE values remained relatively high (Fig. S3).
Except for climatic layers, remote sensing-based layers such as NDVI could be useful for modelling the signal differences in
510   vegetated areas. NDVI reflects the vegetation growth condition, which is the result of several environmental factors interacting.
NDVI therefore contains multiple environmental information. In addition, aerosol could be a contributing factor to the signal
differences, especially in deserts such as the Sahara Desert where the rRMSE values in the final CScat data set remained
relatively high (Fig. S3). The Sentinel 5P mission provides near real-time, high-resolution aerosol products starting from the
year of 2018 (Ingmann et al., 2012). Analysis will soon be conducted to assess whether NDVI and aerosol layers can further
515   improve the data merging quality.

Another potentially useful data set to be included into our data merging framework is the Oceansat-2 scatterometer (OSCAT).
OSCAT also provides Ku-band backscatters akin to QSCAT, but operating in a different period (between 2009 and 2014)
(Bhowmick et al., 2013). QSCAT operated in full mode between 1999 and 2009, and overlapped with ASCAT during three
years (2007-2009). Adding OSCAT will expand the overlapping period by five years (up to 2014), which could help further
520   improve the data merging method.

In Tao et al. (2022b), linear regression was established to predict the signal differences from monthly rainfall amounts, because
the signal differences exhibited a good linear relationship with rainfall in tropical rainforest regions. However, decision tree
regression was used for a limited number of pixels mainly located in the ever-wet north-western Amazonia and Asian tropical
525   rainforests, because the relationship between signal differences and rainfall in these regions is non-linear. The present study
used only the decision tree regression (Fig. 4b, e, h), to increase the model of the signal differences. The use of decision tree
was inspired by Sankaran et al. (2005) in which decision tree was used to dissect the relationship between rainfall and woody
cover for African savannas. More advanced machine learning techniques are an option in the future. Meanwhile, all the three
climatic variables (precipitation, skin temperature, and snow depth) will be used together in one regression model for predicting
530   the signal differences. Currently we built three regression models, each taking one climatic variable as input. As discussed
above, precipitation, skin temperature, and snow depth could be responsible for the signal differences in separate periods.
Multiple variable regression is therefore a promising way to further improve the modelling accuracy.

535   We also plan to generate a new version of radar data set by merging only QSCAT and ASCAT images. Although this will
shorten the time span by a few years, the BYU data centre provides QSCAT and ASCAT images at the resolution of 4.45 km,
thus this new data set will have the advantage of having even higher resolution.

C-band radar data have been widely used in earth science studies for monitoring vegetation dynamics, mapping deforestation
540   and soil moisture, and estimating snow water-equivalent (Chang et al., 1982; Clifford, 2010; Kelly et al., 2003; Liu et al., 2009;
Saatchi et al., 2013; Steele-Dunne et al., 2017; Smith and Bookhagen, 2018). Thus, the merged radar signals are expected to
be useful in a range of research disciplines. A possible outcome is to separate the signal into soil moisture and vegetation

components using radiative transfer models (Liu et al., 2021). This way, the signals can be more directly related to the soil or vegetation dynamics. The merged radar signals span a long time (since 1992), and can be further extended because ASCAT is

545 still operational. Thus, once soil and vegetation signals are separated, the vegetation part would be suitable for assessment of long-term global vegetation changes. Using optical MODIS Leaf Area Index data, a recent study found that most of the world's vegetated areas are becoming greener, particularly in China and India (Chen et al., 2019). Using optical vegetation index NDVI, another recent research explored the long-term (2000-2020) resilience change of global forests (Forzieri et al., 2022). It would be interesting to re-evaluate the vegetation trends using radar data. While radar signal penetrates the upper forest

550 canopy and interacts directly with the water molecules contained in forest biomass, optical greenness data reflect the canopy features of the top-most leaf layer which could be maintained due to leaf demography or light availability (Guan et al., 2015; Wu et al., 2016). We therefore expect the CScat data set to provide new insights into the long-term changes of global forests.

Data availability

555 The CScat data set can be downloaded at https://doi.org/10.6084/m9.figshare.20407857.

Author contribution

S.T. designed the research. S.T. and A.Z. analysed the data, with input from other authors. Y.Y.L. designed the new signal rescaling method. S.T., J.P.W, S.S., P.C., J.C., T. L., and P.L.F. wrote the manuscript. All authors interpreted the results and edited the text.

560 **Competing interests**

The authors declare no competing interests.

Acknowledgements

We thank the BYU data center and Dr. David Long for providing the enhanced-resolution radar images. This work was supported by the National Natural Science Foundation of China (grant no. 31988102); the Strategic Priority Research Program

565 of the Chinese Academy of Sciences Grant XDA26010303; French grants (CEBA, ref. ANR-10-LABX-25-01; TULIP, ref. ANR-10-LABX-0041; ANAEE-France: ANR-11-INBS-0001); CNES postdoctoral fellowship to S.T.; and ESA CCI-BIOMASS.

References

Bhowmick, S. A., Kumar, R., and Kumar, A. K.: Cross calibration of the OceanSAT-2 scatterometer with QuikSCAT scatterometer using natural terrestrial targets, IEEE Trans. Geosci. Remote Sens., 52, 3393-3398, 2013.

Brocca, L., Hasenauer, S., Lacava, T., Melone, F., Moramarco, T., Wagner, W., Dorigo, W., Matgen, P., Martínez-Fernández, J., and Llorens, P.: Soil moisture estimation through ASCAT and AMSR-E sensors: An intercomparison and validation study across Europe, Remote Sens. Environ., 115, 3390-3408, 2011.

Camberlin, P., Barraud, G., Bigot, S., Dewitte, O., Makanzu Imwangana, F., Maki Mateso, J. C., Martiny, N., Monsieurs, E., Moron, V., and Pellarin, T.: Evaluation of remotely sensed rainfall products over Central Africa, Q. J. R. Meteorol. Soc., 145, 2115-2138, 2019.

Carabajal, C. C. and Harding, D. J.: SRTM C-band and ICESat laser altimetry elevation comparisons as a function of tree cover and relief, Photogramm. Eng. Remote Sens., 72, 287-298, 2006.

Chang, A. T., Foster, J. L., Hall, D. K., Rango, A., and Hartline, B. K.: Snow water equivalent estimation by microwave radiometry, Cold Reg. Sci. Technol., 5, 259-267, 1982.

Chen, C., Park, T., Wang, X., Piao, S., Xu, B., Chaturvedi, R. K., Fuchs, R., Brovkin, V., Ciais, P., and Fensholt, R.: China and India lead in greening of the world through land-use management, Nat. Sustain., 2, 122-129, 2019.

Clifford, D.: Global estimates of snow water equivalent from passive microwave instruments: history, challenges and future developments, Int. J. Remote Sens., 31, 3707-3726, 2010.

Crapolicchio, R., De Chiara, G., Elyouncha, A., Lecomte, P., Neyt, X., Paciucci, A., and Talone, M.: ERS-2 scatterometer: Mission performances and current reprocessing achievements, IEEE Trans. Geosci. Remote Sens., 50, 2427-2448, 2012.

Du, J., Kimball, J. S., Jones, L. A., Kim, Y., Glassy, J., and Watts, J. D.: A global satellite environmental data record derived from AMSR-E and AMSR2 microwave Earth observations, Earth Syst. Sci. Data, 9, 791-808, 2017.

Early, D. S. and Long, D. G.: Image reconstruction and enhanced resolution imaging from irregular samples, IEEE Trans. Geosci. Remote Sens., 39, 291-302, 2001.

Figa-Saldaña, J., Wilson, J. J., Attema, E., Gelsthorpe, R., Drinkwater, M. R., and Stoffelen, A.: The advanced scatterometer (ASCAT) on the meteorological operational (MetOp) platform: A follow on for European wind scatterometers, Can. J. Remote Sens., 28, 404-412, 2002.

Forzieri, G., Dakos, V., McDowell, N. G., Ramdane, A., and Cescatti, A.: Emerging signals of declining forest resilience under climate change, Nature, 1-6, 2022.

Frappart, F., Fatras, C., Mougin, E., Marieu, V., Diepkilé, A., Blarel, F., and Borderies, P.: Radar altimetry backscattering signatures at Ka, Ku, C, and S bands over West Africa, Phys. Chem. Earth, 83, 96-110, 2015.

Frison, P.-L. and Mougin, E.: Use of ERS-1 wind scatterometer data over land surfaces, IEEE Trans. Geosci. Remote Sens., 34, 550-560, 1996.

Gelaro, R., McCarty, W., Suárez, M. J., Todling, R., Molod, A., Takacs, L., Randles, C. A., Darmenov, A., Bosilovich, M. G., and Reichle, R.: The modern-era retrospective analysis for research and applications, version 2 (MERRA-2), J. Clim., 30, 5419-5454, 2017.

605 Guan, K., Pan, M., Li, H., Wolf, A., Wu, J., Medvigy, D., Caylor, K. K., Sheffield, J., Wood, E. F., and Malhi, Y.: Photosynthetic seasonality of global tropical forests constrained by hydroclimate, Nat. Geosci., 8, 284-289, 2015.

Iguchi, T., Kozu, T., Meneghini, R., Awaka, J., and Okamoto, K. i.: Rain-profiling algorithm for the TRMM precipitation radar, J. Appl. Meteorol., 39, 2038-2052, 2000.

Ingmann, P., Veihelmann, B., Langen, J., Lamarre, D., Stark, H., and Courrèges-Lacoste, G. B.: Requirements for the GMES

610 Atmosphere Service and ESA's implementation concept: Sentinels-4/-5 and-5p, Remote Sens. Environ., 120, 58-69, 2012.

Kelly, R. E., Chang, A. T., Tsang, L., and Foster, J. L.: A prototype AMSR-E global snow area and snow depth algorithm, IEEE Trans. Geosci. Remote Sens., 41, 230-242, 2003.

Kobayashi, K. and Salam, M. U.: Comparing simulated and measured values using mean squared deviation and its components, Agron. J., 92, 345-352, 2000.

615 Konings, A. G., Yu, Y., Xu, L., Yang, Y., Schimel, D. S., and Saatchi, S. S.: Active microwave observations of diurnal and seasonal variations of canopy water content across the humid African tropical forests, Geophys. Res. Lett., 44, 2290-2299, 2017.

Le Toan, T., Quegan, S., Davidson, M., Balzter, H., Paillou, P., Papathanassiou, K., Plummer, S., Rocca, F., Saatchi, S., and Shugart, H.: The BIOMASS mission: Mapping global forest biomass to better understand the terrestrial carbon cycle,

620 Remote Sens. Environ., 115, 2850-2860, 2011.

Lecomte, P. and Wagner, W.: ERS wind scatterometer commissioning & in-flight calibration, European Space Agency-Publications-ESA SP, 424, 261-270, 1998.

Liu, X., Wigneron, J.-P., Fan, L., Frappart, F., Ciais, P., Baghdadi, N., Zribi, M., Jagdhuber, T., Li, X., and Wang, M.: ASCAT IB: A radar-based vegetation optical depth retrieved from the ASCAT scatterometer satellite, Remote Sens. Environ.,

625 264, 112587, 2021.

Liu, Y. Y., van Dijk, A. I., de Jeu, R. A., and Holmes, T. R.: An analysis of spatiotemporal variations of soil and vegetation moisture from a 29-year satellite-derived data set over mainland Australia, Water Resour. Res., 45, 2009.

Liu, Y. Y., De Jeu, R. A., McCabe, M. F., Evans, J. P., and Van Dijk, A. I.: Global long-term passive microwave satellite-based retrievals of vegetation optical depth, Geophys. Res. Lett., 38, 2011.

630 Long, D. G., Hardin, P. J., and Whiting, P. T.: Resolution enhancement of spaceborne scatterometer data, IEEE Trans. Geosci. Remote Sens., 31, 700-715, 1993.

Malenovský, Z., Rott, H., Cihlar, J., Schaepman, M. E., García-Santos, G., Fernandes, R., and Berger, M.: Sentinels for science: Potential of Sentinel-1,-2, and-3 missions for scientific observations of ocean, cryosphere, and land, Remote Sens. Environ., 120, 91-101, 2012.

635   Moesinger, L., Dorigo, W., de Jeu, R., van der Schalie, R., Scanlon, T., Teubner, I., and Forkel, M.: The global long-term
          microwave vegetation optical depth climate archive (VODCA), Earth Syst. Sci. Data, 12, 177-196, 2020.

Muñoz-Sabater, J.: ERA5-Land monthly averaged data from 1981 to present, Copernicus Climate Change Service (C3S)
          Climate Data Store (CDS) [data set], https://doi.org/10.24381/cds.68d2bb3, 2019.

Murfitt, J. and Duguay, C. R.: 50 years of lake ice research from active microwave remote sensing: Progress and prospects,
640   Remote Sens. Environ., 264, 112616, 2021.

Naeimi, V., Paulik, C., Bartsch, A., Wagner, W., Kidd, R., Park, S.-E., Elger, K., and Boike, J.: ASCAT Surface State Flag
          (SSF): Extracting information on surface freeze/thaw conditions from backscatter data using an empirical threshold-
          analysis algorithm, IEEE Trans. Geosci. Remote Sens., 50, 2566-2582, 2012.

Orsolini, Y., Wegmann, M., Dutra, E., Liu, B., Balsamo, G., Yang, K., de Rosnay, P., Zhu, C., Wang, W., and Senan, R.:
645   Evaluation of snow depth and snow cover over the Tibetan Plateau in global reanalyses using in situ and satellite remote
          sensing observations, Cryosphere, 13, 2221-2239, 2019.

Prigent, C., Matthews, E., Aires, F., and Rossow, W. B.: Remote sensing of global wetland dynamics with multiple satellite
          data sets, Geophys. Res. Lett., 28, 4631-4634, 2001.

Prigent, C., Jimenez, C., Dinh, L. A., Frappart, F., Gentine, P., Wigneron, J. P., and Munchak, J.: Diurnal and Seasonal
650   Variations of Passive and Active Microwave Satellite Observations Over Tropical Forests, J. Geophys. Res.: Biogeosci.,
          127, e2021JG006677, 2022.

Pulliainen, J., Luojus, K., Derksen, C., Mudryk, L., Lemmetyinen, J., Salminen, M., Ikonen, J., Takala, M., Cohen, J., and
          Smolander, T.: Patterns and trends of Northern Hemisphere snow mass from 1980 to 2018, Nature, 581, 294-298, 2020.

Saatchi, S., Asefi-Najafabady, S., Malhi, Y., Aragão, L. E., Anderson, L. O., Myneni, R. B., and Nemani, R.: Persistent effects
655   of a severe drought on Amazonian forest canopy, Proc. Natl. Acad. Sci. U.S.A., 110, 565-570, 2013.

Sankaran, M., Hanan, N. P., Scholes, R. J., Ratnam, J., Augustine, D. J., Cade, B. S., Gignoux, J., Higgins, S. I., Le Roux, X.,
          and Ludwig, F.: Determinants of woody cover in African savannas, Nature, 438, 846-849, 2005.

Shi, J., Xiong, C., and Jiang, L.: Review of snow water equivalent microwave remote sensing, Sci. China Earth Sci., 59, 731-
          745, 2016.

660   Smith, T. and Bookhagen, B.: Changes in seasonal snow water equivalent distribution in High Mountain Asia (1987 to 2009),
          Sci. Adv., 4, e1701550, 2018.

Spreen, G., Kaleschke, L., and Heygster, G.: Sea ice remote sensing using AMSR-E 89-GHz channels, J. Geophys. Res.:
          Oceans, 113, 2008.

Steele-Dunne, S. C., McNairn, H., Monsivais-Huertero, A., Judge, J., Liu, P.-W., and Papathanassiou, K.: Radar remote
665   sensing of agricultural canopies: A review, IEEE J. Sel. Top. Appl. Earth Obs. Remote Sens., 10, 2249-2273, 2017.

Tao, S., Ao, Z., Wigneron, J.-P., Saatchi, S., Ciais, P., Chave, J., Le Toan, T., Frison, P.-L., Hu, X., Chen, C., Fan, L., Wang,
          M., Zhu, J., Zhao, X., Li, X., Liu, X., Su, Y., Hu, T., Guo, Q., Wang, Z., Tang, Z., Liu, Y.Y., Fang, J. C-band Scatterometer

(CScat): the first global long-term satellite radar backscatter data set with a C-band signal dynamic, Figshare [CScat data set], https://doi.org/10.6084/m9.figshare.20407857, 2022a.

670 Tao, S., Chave, J., Frison, P.-L., Toan, T. L., Ciais, P., Fang, J., Wigneron, J.-P., Santoro, M., Yang, H., Li, X., Labrière, N., and Saatchi, S.: Increasing and widespread vulnerability of intact tropical rainforests to repeated droughts, Proc. Natl. Acad. Sci. U.S.A., accecpted., 2022b.

Tsai, W. T., Spencer, M., Wu, C., Winn, C., and Kellogg, K.: SeaWinds on QuikSCAT: sensor description and mission overview, IEEE 2000 International Geoscience and Remote Sensing Symposium, Honolulu Hawaii, 24-28 July 2000,
675 10.1109/IGARSS.2000.858008, 2000.

Ulaby, F., Moore, R., and Fung, A.: Microwave remote sensing: Active and passive. Volume 2-Radar remote sensing and surface scattering and emission theory, Addison-Wesley Advanced Book Program: Reading, Massachusetts, 1982.

Ulaby, F. T., Long, D. G., Blackwell, W. J., Elachi, C., Fung, A. K., Ruf, C., Sarabandi, K., Zebker, H. A., and Van Zyl, J.: Microwave radar and radiometric remote sensing, University of Michigan Press Ann Arbor, MI, USA, 2014.

680 Wagner, W., Lemoine, G., Borgeaud, M., and Rott, H.: A study of vegetation cover effects on ERS scatterometer data, IEEE Trans. Geosci. Remote Sens., 37, 938-948, 1999.

Wagner, W., Blöschl, G., Pampaloni, P., Calvet, J.-C., Bizzarri, B., Wigneron, J.-P., and Kerr, Y.: Operational readiness of microwave remote sensing of soil moisture for hydrologic applications, Hydrol. Res., 38, 1-20, 2007.

Wang, M., Wigneron, J.-P., Sun, R., Fan, L., Frappart, F., Tao, S., Chai, L., Li, X., Liu, X., and Ma, H.: A consistent record
685 of vegetation optical depth retrieved from the AMSR-E and AMSR2 X-band observations, Int. J. Appl. Earth Obs. Geoinf., 105, 102609, 2021.

Weissman, D., Stiles, B., Hristova-Veleva, S., Long, D., Smith, D., Hilburn, K., and Jones, W.: Challenges to satellite sensors of ocean winds: Addressing precipitation effects, J. Atmos. Ocean Technol., 29, 356-374, 2012.

Wentz, F. J.: Measurement of oceanic wind vector using satellite microwave radiometers, IEEE Trans. Geosci. Remote Sens.,
690 30, 960-972, 1992.

Wigneron, J.-P., Jackson, T., O'neill, P., De Lannoy, G., de Rosnay, P., Walker, J., Ferrazzoli, P., Mironov, V., Bircher, S., and Grant, J.: Modelling the passive microwave signature from land surfaces: A review of recent results and application to the L-band SMOS & SMAP soil moisture retrieval algorithms, Remote Sens. Environ., 192, 238-262, 2017.

Wigneron, J.-P., Li, X., Frappart, F., Fan, L., Al-Yaari, A., De Lannoy, G., Liu, X., Wang, M., Le Masson, E., and Moisy, C.:
695 SMOS-IC data record of soil moisture and L-VOD: Historical development, applications and perspectives, Remote Sens. Environ., 254, 112238, 2021.

Wu, J., Albert, L. P., Lopes, A. P., Restrepo-Coupe, N., Hayek, M., Wiedemann, K. T., Guan, K., Stark, S. C., Christoffersen, B., and Prohaska, N.: Leaf development and demography explain photosynthetic seasonality in Amazon evergreen forests, Science, 351, 972-976, 2016.

700 Yao, P., Lu, H., Shi, J., Zhao, T., Yang, K., Cosh, M. H., Gianotti, D. J., and Entekhabi, D.: A long term global daily soil moisture dataset derived from AMSR-E and AMSR2 (2002–2019), Sci. Data, 8, 1-16, 2021.

Zhang, H., Zhang, F., Che, T., Yan, W., and Ye, M.: Investigating the ability of multiple reanalysis datasets to simulate snow depth variability over mainland China from 1981 to 2018, J. Clim., 34, 9957-9972, 2021.